ADVANCED FUNCTIONAL MATERIALS

FULL PAPER

DOI: 10.1002/adfm.200700459

Charge Transport through Oligoarylene Self-assembled Monolayers: Interplay of Molecular Organization, Metal–Molecule Interactions, and Electronic Structure**

By *Christian Grave*, *Chad Risko*, *Andrey Shaporenko*, *Yiliang Wang*, *Colin Nuckolls*, *Mark A. Ratner*, *Maria Anita Rampi*,* and *Michael Zharnikov**

The electrical properties of two molecular wires-a novel aryl moiety, 6-(5-pyridin-2-ylpyrazin-2-yl)pyridine-3-thiol (PPPT), and the well studied 1,1';4',1''-terphenyl-4-thiol (TPT)-organized in self-assembled monolayers (SAMs) are measured using metal–molecule–metal (MMM) mercury-drop junctions. Current measured at the same bias voltage through PPPT is found to be more than one order of magnitude lower than through TPT. To interpret and understand these results, characterization of the structure, organization of the SAMs, and theoretical analyses of the molecular systems are discussed. X-ray photoelectron spectroscopy (XPS) and near-edge X-ray absorption fine structure spectroscopy (NEXAFS) indicate that although PPPT forms high-quality SAMs on both Au and Ag substrates, it exhibits a lower packing density (by 20 %) and less orientational order than TPT. In addition, electronic structure calculations with density functional theory (DFT) reveal that the electron-withdrawing nitrogen atoms in the PPPT aryl backbone stabilize the valence molecular electronic structure and pull negative charge from the thiol sulfur. This behavior can influence both charge-injection barriers and metal–molecule binding interactions in the MMM junctions. The current–voltage data are interpreted on the basis of a hole-tunneling, through-bond mechanism. Conductance analysis through a model for off-resonant tunneling transport suggests that a comparatively small difference in the charge-injection barrier can explain the factor of ten difference in observed conduction.

1. Introduction

Organic compounds–either as single molecules or organized in self-assembled monolayers (SAMs)–can act as wires, rectifiers, switches, or even transistors in the development of ultra-miniaturized electronics.[1–2] The prospect of such *molecular electronics* has led to a steadily growing interest in the characterization of both the electronic and structural features of relevant molecular species bound to metal substrates. Specifically, measurements and theoretical simulations of current–voltage (I–V) relationships aimed at describing how electronic and structural properties correlate with conductance have increased dramatically over the past few years.[2–8]

A variety of metal–molecule–metal (MMM) junctions have been developed to empirically probe these characteristics. In addition to techniques that aim to measure electrical properties of a single molecule (e.g., break junctions)[9–14] or a few molecules (e.g., STM-based methods),[15–18] large area MMM junctions involving an ordered assembly of molecules (i.e., SAMs) on a conducting metal or semiconductor substrate have become quite popular because of their generally simple design.[19–24] Even though the electrical properties of such junctions are mostly associated with the chemical structure of the individual molecules, the impact of the organization[25] of the molecules in SAMs sandwiched between two electrodes[26] is an important parameter in understanding the charge transport characteristics. Whereas electronic delocalization along the molecular backbone is considered a fundamental characteristic in obtaining high molecular conductance, effects related to the molecular organization in monolayers are seldom discussed; of particular importance are i) the binding of the molecular headgroup to the surface,[23] ii) the degree of order in the SAMs,

[*] Dr. M. Zharnikov, Dr. A. Shaporenko
Angewandte Physikalische Chemie
Universitat Heidelberg, Heidelberg 69120 (Germany)
E-mail: Michael.Zharnikov@urz.uni-heidelberg.de
Prof. M. A. Rampi, Dr. C. Grave
Dipartimento di Chimica, Via Borsari 46
Università di Ferrara, Ferrara 44100 (Italy)
E-mail: rmp@unife.it
Dr. C. Risko, Prof. M. A. Ratner
Department of Chemistry and Materials Research Center
Northwestern University
Evanston, IL 60208 (USA)
Y. Wang, Prof. C. Nuckolls
Department of Chemistry and The Nanoscience Center
Columbia University
New York, NY 10027 (USA)

[**] We thank M. Grunze for support of this work, Ch. Wöll for providing us with the experimental equipment for the spectroscopic measurements, and the BESSY II staff for assistance during the synchrotron-based experiments. C. R. would like to thank G. Solomon and M. Sukharev for fruitful discussions. This work has been supported by the German BMBF (05 KS4VHA/4), DFG (ZH 63/9-2), the European Union through the Project Contract IST-2001-35503 (LIMM), and the NSF through the Northwestern University MRSEC (DMR-0076097) and NSF International Division. Supporting Information is available online from Wiley InterScience or from the author.

© 2007 WILEY-VCH Verlag GmbH & Co. KGaA, Weinheim

ADVANCED FUNCTIONAL MATERIALS

and iii) the orientation and conformation of the molecular backbone(s).[17,18,25,27] The latter parameters are especially critical for complex molecules that may adopt a number of very different orientations and conformations on the surface. Whereas an increasing number of studies deal with electrical measurements of different molecules and their respective SAMs, systematic investigations to deduce the influence of molecular environment on the electrical properties of such systems are scarce (see, e.g., ref. 25).

Here we present structural and transport characteristics of SAMs formed from a novel molecular wire, 6-(5-pyridin-2-yl-pyrazin-2-yl)pyridine-3-thiol (PPPT, Fig. 1), on Au and Ag substrates to probe the effects of heteroatom substitution in the aryl backbone of oligophenylene-based molecules on their relatively high electrical conductance properties;[8,17,18] specifically, we are interested in comparisons with the structurally analogous 1,1';4',1''-terphenyl-4-thiol (TPT). PPPT is also of relevance in that it can undergo conformational rearrangement of the pyridine and pyrazine units to form two 2,2'-bipyridyl motifs that can act as ligands for the incorporation of different metal complexes into the SAM; this aspect is particularly fascinating as incorporating metal-centered redox sites into the molecular wire can have an intriguing role in mediating electron transfer processes, an issue we will address in future work. The structural and electronic properties of PPPT SAMs were studied by X-ray photoelectron spectroscopy (XPS) and near edge X-ray absorption fine structure (NEXAFS) spectroscopy; a detailed analysis of the structure and properties of TPT SAMs can be found elsewhere.[28-30] The *I–V* characteristics of PPPT SAMs were measured with a mercury-based MMM junction and compared with previously published results for TPT films.[31] In addition, *I–V* measurements through dodecanethiolate (DDT) SAMs were also reported as a reference for current flowing through molecules of similar length and substantially different electronic structure. The experimental data are analyzed on the basis of theoretical calculations performed within the density functional theory (DFT) framework and modeled with a conduction model for off-resonant tunneling transport.

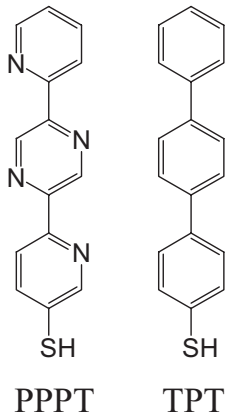

Figure 1. The molecular structures of PPPT and TPT.

2. Results

2.1. XPS and NEXAFS Characterization

Both XPS and NEXAFS data suggest that films prepared from a 0.3 mM solution of the PPPT precursor have a superior quality compared to SAMs fabricated from a 20 μM solution. The latter films exhibited no orientational order and were partly contaminated; in particular, a pronounced O 1s emission was observed in the XPS spectra of these films, whereas the respective NEXAFS data showed a clear fingerprint of the C=O moieties. Therefore, we solely present and discuss data for SAMs prepared from the 0.3 mM solution of the target compounds. No pronounced differences between the spectra of PPPT/Au and PPPT/Ag were observed; thus, only data for PPPT/Au will be shown.

The S 2p, C 1s, and N 1s XPS spectra of PPPT/Au are shown in Figure 2. The relatively poor signal-to-noise ratio of the S 2p spectrum is explained by the attenuation of the corresponding signal by the SAM overlayer and the relatively short acquisition time chosen to reduce possible X-ray-induced damage during the measurements.[32–35] The comparatively poor signal-to-noise ratio of the N 1s spectrum stems from the large inelastic background in this binding energy (BE) range and the low photoionization cross section of the N 1s core level at the given photon energy.[36–38]

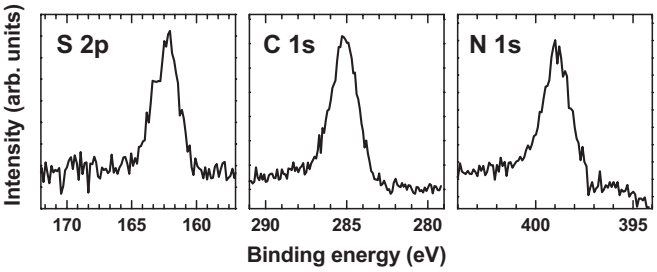

Figure 2. S 2p, C 1s, and N 1s XPS spectra of PPPT/Au acquired at photon energies of 440 eV (S 2p) and 660 eV (C 1s and N 1s).

In the S 2p spectrum, a single S $2p_{3/2}/2p_{1/2}$ doublet was observed at a BE of 162.2 eV for both PPPT/Au and PPPT/Ag. This doublet, typical for intact thiol-derived SAMs, is usually associated with a thiolate species bound to the metal surface.[39-41] With the exception of the doublet, no further features, including emissions related to atomic sulfur, disulfides, alkylsulfides, or oxidative products of sulfur, were observed. The BE of the S 2p doublet in the PPPT films was somewhat larger than the analogous values for biphenyl- and terphenylthiolate SAMs (162.0–162.1 eV),[28,30,40] which indicate a partial withdrawal of negative charge from the metal–thiolate bond to the pyridine and pyrazine rings because of the higher electronegativity of nitrogen compared to carbon (see below).

In the C 1s spectrum, a single C 1s emission was observed at a BE of 285.1 for both PPPT/Au and PPPT/Ag; no "fine structure" could be resolved, and emissions related to carbon mon-

© 2007 WILEY-VCH Verlag GmbH & Co. KGaA, Weinheim

oxide or dioxide were not exhibited. This band is attributed to carbon in the pyridine/pyrazine backbone. The BE of the major C 1s emission in the PPPT films was noticeably higher than the analogous value for biphenyl- and terphenylthiolate SAMs (ca. 284.1 eV).[28,30,40] These results point to the aryl carbon atoms being more positively charged upon substitution of the nitrogen atoms into the backbone (see below). Such a shift has been observed in pyridine-terminated SAMs on Au substrates, in which the C 1s emissions related to the carbon atoms in the *ortho* and *para* positions of the pyridine were observed at 285.3–286.6 eV.[42]

A single emission in the N 1s spectrum related to nitrogen atom incorporation into the aromatic rings is observed at a BE of 399.0 eV for both PPPT/Au and PPPT/Ag. This BE is very close to the value expected for an unmodified pyridine moiety (ca. 399.0 eV)[42] and is slightly smaller than the value for so-called "weakly" H-bonded pyridine (399.1–399.5 eV).[42] At the same time, it is noticeably smaller than the value for "strongly" H-bonded pyridine (400.4–400.9 eV)[42] and protonated pyridine (401.4–402.4 eV).[42,43] Thus, the PPPT molecules in the respective SAMs contain mostly unmodified pyridine moieties, and there is, at most, "weak" H-bonding between the neighboring molecules in the SAM.

The O 1s spectrum (not shown) indicates that there was a small amount of oxygen contamination for both PPPT/Au and PPPT/Ag. Emission in the spectrum was assigned to residual C=O species, which were not removed from the substrate surface during SAM formation. The "self-cleaning" of C=O worked quite well in the case of alkanethiolate or biphenylthiolate SAMs but was not complete in the present case. This effect could be related to a weakening of the thiolate–substrate bond because of a partial withdrawal of negative charge by the molecular backbone; specifically, it was assumed that the identity of the 4'-substituent in SAMs of 4-mercaptobiphenyls could affect the adsorption kinetics as well as the equilibrium structure of these bound structures.[44,45]

On the basis of the XPS data, the effective thickness of the PPPT films could be estimated using a standard expression for an exponential attenuation of the photoemission signal and attenuation lengths for densely packed hydrocarbons.[46] For the evaluation, we used the ratios of the C1s/Au4f and C1s/Ag3d emissions[47] and performed, as an additional check, similar calculations for *n*-alkanethiolate SAMs on Au and Ag, which were in good agreement with literature values.[48] The thickness of the PPPT film was estimated to be 13.9 and 13.5 Å on Au and Ag, respectively. These values are fairly close to the sum of the molecular lengths of PPPT (14.2 Å) and substrate–S distances (2.4 Å),[49] which suggest an upright orientation and a dense packing of these molecules in the respective SAMs. Considering that the estimated thicknesses were somewhat smaller than the above sum, a slight molecular inclination can be assumed. Taking into account the similar molecular lengths of the PPPT and TPT molecules, comparison of the derived effective thicknesses of the PPPT films with the analogous values for the TPT SAMs (15.3 and 16.5 Å for Au and Ag, respectively)[28,30] suggests that the packing density of the PPPT films was approximately 80–85 % of the packing density found for TPT SAMs.

Information from NEXAFS spectra complemented the XPS data. In the NEXAFS experiment, core level electrons (e.g., C 1s for a C K-edge spectrum) were excited into the unoccupied molecular orbitals characteristic for a specific bond, functional group, or molecule; the photon energy positions of the respective absorption resonances provided a clear signature of these entities. In addition, information on molecular orientation could be derived, as the cross section of the resonant photoexcitation process depends on the orientation of the electric field vector of the linearly polarized synchrotron light with respect to the molecular orbital of interest (so-called linear dichroism in X-ray absorption) and is a maximum if the direction of the **E**-vector and the transition dipole moment (TDM) of the orbital are collinear.[50] For analysis of the spectral features, however, it is useful to exclude effects of molecular orientation. For this purpose, a spectrum acquired at the so called *magic angle* of light incidence (ca. 55°) is most suitable, as it is independent of the molecular orientation.[50]

The C K-edge NEXAFS spectra of PPPT/Au acquired at X-ray incidence angles of 20°, 55°, and 90°, as well as the respective difference spectrum (i.e., the difference between the spectra acquired at 90° and 20°), are presented in Figure 3. Assignments and energy positions of the absorption

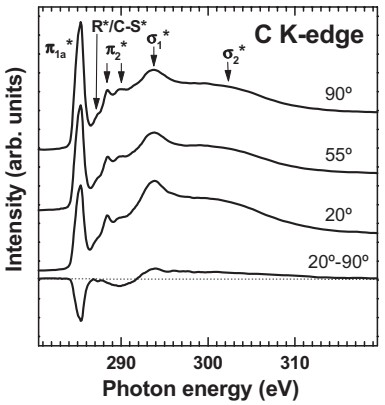

Figure 3. Normalized carbon K-edge NEXAFS spectra of PPPT/Au acquired at X-ray incidence angles of 90°, 55°, and 20°, along with the respective 20°–90° difference spectrum. The characteristic absorption resonances are marked (see text and Table 1).

resonances are given in Table 1, along with analogous data for benzene,[50–53] pyridine,[53,54] pyrazine,[54,55] and TPT/Au;[30] benzene is considered as a general reference for aromatic compounds, whereas the pyridine and pyrazine data serve as references for the structural components of PPPT. Note that the shape of the C K-edge NEXAFS spectrum for both pyridine and pyrazine is very similar to benzene.

We find that the general shape of the C K-edge NEXAFS spectrum for PPPT/Au is also similar to the spectrum for benzene.[50,53] The spectrum exhibits a C 1s absorption edge related to C 1s → continuum excitations located at ca. 287 eV[56] and several π^* and σ^* resonances. The spectra are dominated by a strong, slightly asymmetric π_1^* resonance at 285.35 eV, which is accompanied by a weaker π_2^* resonance at ca. 289.7 eV. The

© 2007 WILEY-VCH Verlag GmbH & Co. KGaA, Weinheim

ADVANCED FUNCTIONAL MATERIALS

Table 1. Photon energy positions (eV) and assignments (only the final orbital) of the C K-edge NEXAFS resonances for PPPT SAMs on Au and Ag along with reference data for benzene,[50–53] pyridine,[53,54[pyrazine,[54,55] and TPT/Au.[30]

	π_{1a}*	R*/C-S*	π_2*	σ_1*	σ_2*	Step
Assignment for benzene [a]	$\pi^*(e_{2u})$		$\pi^*(b_{2g})$	$\sigma^*(e_{1u})$	$\sigma^*(e_{2g}+a_{2g})$	
Benzene (solid phase)	285.0		288.9	293.3	300.1	284.9
Pyridine [a] (solid phase)	285.0 (b_1) + 285.6 (a_2)		289.1	294.1	301	284.4
Pyrazine [a] (solid phase)	285.3 (b_{3u}) + 286.1 (a_u)		291.2	297.4	306.0	
TPT/Au	285.0	287.4	288.9	293.0	300.0	
PPPT	285.35	287.3	288.45 + 289.8	293.8	302.0	

[a] The $\pi^*(e_{2u})$ resonance is split into two peaks in pyridine and pyrazine.

broad resonances at ca. 293.9 and ca. 300 eV are related to transitions into σ^* orbitals.[50,51,53] The value of 285.35 eV lies exactly between the positions of the $\pi_1^*(b_1)$ and $\pi_1^*(a_2)$ resonances in pyridine (which are merged at the given energy resolution) and is very close to the position of the $\pi_1^*(b_{3u})$ resonance in pyrazine. The $\pi_1^*(a_u)$ resonance of pyrazine is not distinguishable. Compared to the π_1^* resonance position in benzene (285.0 eV),[53] the observed shift of 0.35 eV is predominately the result of a shift in the C 1s core level between benzene and pyridine/pyrazine. The asymmetry of the π_1^* resonance in the PPPT films is presumably related to the multicomponent character of this resonance, which is a superposition of at least three components [($\pi_1^*(b_1)$, $\pi_1^*(a_2)$, and $\pi_1^*(b_{3u})$] with different spectral weights.

The N K-edge NEXAFS spectra of the PPPT films are quite similar to those of pyridine[53,54,57,58] and pyrazine.[54,55] One such spectrum (55°) for PPPT/Au is presented in Figure 4. The assignments and energy positions of the absorption resonances

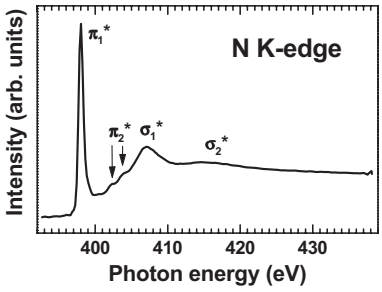

Figure 4. Normalized nitrogen K-edge NEXAFS spectrum of PPPT/Au acquired at an X-ray incidence angle of 55°. The characteristic absorption resonances are marked (see text and Table 2).

are given in Table 2, along with the analogous data for pyridine and pyrazine presented for comparison. The spectra are dominated by a pronounced π^* resonance at 398.1 eV, which is accompanied by weak π^*-like features at 402.3 and 403.8 eV and broad σ^* resonances at 407.1 and 415.6 eV.

In addition to sampling unoccupied molecular orbitals, NEXAFS data provided information on both orientation and orientational order of the PPPT films. The C K-edge spectrum

Table 2. Photon energy positions (eV) and assignments (only the final orbital) of the N K-edge NEXAFS resonances for the PPPT SAMs on Au and Ag along with the reference data for pyridine[53,54] and pyrazine.[54,55]

	π_1*	π_2*	σ_1*	σ_2*
Pyridine (solid phase)	399.0 (b_1)	403.3	408	414.3
Pyrazine (solid phase)	399.3 (b_{3u})	406	411.1	417.6
PPPT	398.1	402.3 + 403.8	407.1	415.6

in Figure 3 exhibits a pronounced linear dichroism; that is, the intensities of the absorption resonances changes significantly when the angle of X-ray incidence is varied. This result implies a relatively high orientational order in the PPPT films. As mentioned above, the intensity of a NEXAFS resonance depends on the orientation of the electric field vector with respect to the TDM of the probed molecular orbital and is maximal if the direction of the **E**-vector and the TDM are collinear. The spectra in Figure 3 exhibit an increase in the π^* resonance intensity and a decrease in the σ^* intensity with increasing angle of light incidence, which implies an upright orientation of the PPPT molecules in the respective SAMs and is a result in full agreement with the XPS data. The inverse behavior of the π^* and σ^* resonance intensities can be explained by the orthogonal orientation of the π^* and σ^* orbitals: whereas the latter orbitals are oriented within the ring plane, the vector-type π^* orbitals are perpendicular to this plane.[50]

In addition to these qualitative considerations, an average tilt angle of the molecules can be estimated by quantitative analysis of the angular dependence of the NEXAFS resonance intensities. For this analysis, the π_1^* resonance was selected, as it is the most intense and distinct feature in the absorption spectra of the films. The numerical evaluation of the derived intensity dependence was performed on the basis of a standard expression for a vector-type orbital[50]

$$I(\alpha) \propto 1 + \quad (3\cos^2\theta - 1)(3\cos^2\alpha - 1) \qquad (1)$$

where α is the average tilt angle of the π_1^* orbitals with respect to the surface normal and θ is the X-ray incidence angle. Equation 1 was slightly modified for the case of the aromatic molecules.[59,60] A herringbone packing of the PPPT backbones with

© 2007 WILEY-VCH Verlag GmbH & Co. KGaA, Weinheim

a twist angle of 32° typical for bulk aromatic compounds was assumed.[56,61,62] As a result, we obtain an average tilt angle of the PPPT aromatic backbone of 32° for PPPT/Au and 35° for PPPT/Ag. The estimated accuracy of these values is about ± 5° (mostly related to an uncertainty in the values of the twist angles). Note that compared to the oligophenylene–thiolate SAMs of the same chain length, that is, TPT SAMs (20° for TPT/Au and 16° for TPT/Ag),[30,39] PPPT exhibited a significantly higher molecular tilt. Note also that the higher value for the average tilt angle of the aromatic backbone in the PPPT film does not definitively suggest that all PPPT molecules are respectively inclined but simply that there is a lower orientational order in this film versus TPT.

2.2. *I–V* Measurements

Taking into consideration the results of the spectroscopic characterization, only films prepared from a 0.3 mM solution of the respective oligoarylenes were used for the *I–V* experiments. Under these conditions, all Au–X//DDT–Hg (X = PPPT, TPT, DDT) junctions were mechanically stable, thus allowing several consecutive and reproducible measurements to be made for each sample. Only a small percentage (5 %) of the assembled junctions showed short circuits, mainly from defects in the SAMs. The *I–V* curves for the Au–X//DDT–Hg (X = PPPT, TPT, DDT) junctions were measured on a statistically significant number of junctions (more than 20 of each type). The average values of I at a given ΔV are reported in Figure 5; the error bars represent a standard deviation from these values.

The *I–V* curves in Figure 5 show symmetric behavior for both a positive and a negative applied bias. Over the entire ΔV range, i) the current measured for TPT was the highest, ii) the current for PPPT was more than one order of magnitude lower that for TPT, and iii) the current for DDT SAM was two orders of magnitude lower than the current measured for TPT.[31] The relatively large errors (error bars in Fig. 5) are typical for this type of junction and are generally related to a combination of statistical error and the error in estimating the area of the junction or the contact area between the solid gold electrode and the Hg-drop electrode.[31] Presumably, there were also some additional disturbance factors in the case of the Au–PPPT//DDT–Hg junction, as the statistical deviation for this junction was larger than for the Au–TPT//DDT–Hg and Au–DDT//DDT–Hg assemblies. However, even accounting for the large experimental error, the higher conductivity of the TPT SAM compared to the PPPT film is unambiguous.

2.3. Computational Results

2.3.1. Geometry

With reference to the atom numbering scheme shown in Figure 6, Table 3 provides selected bond lengths and torsion angles for TPT and PPPT at the B3LYP/6-31G** level of theory. For the gas-phase neutral ground state of TPT, the alternating torsion angle conformer is the most energetically stable, although the energy difference (0.36 kcal mol^{-1}) was not significant. As the bond lengths of the two conformations are virtually the same, the primary difference is in the torsion angles between the phenyl rings: 33.8° and –38.4° for the alternating conformation and 38.2° and 39.3° for the helical conformation. In the case of PPPT, starting the geometric analyses in either the alternating or helical conformation led to the same equilibrium geometry-a virtually planar aryl system. We therefore found that the lowest energy gas-phase conformations of TPT and PPPT were dramatically different, with TPT favoring a twisted conformation and PPPT being planar.

With the distinctions displayed in the preferred equilibrium geometries already apparent, it was of interest to understand if other geometric conformations were realistic, especially for ex-

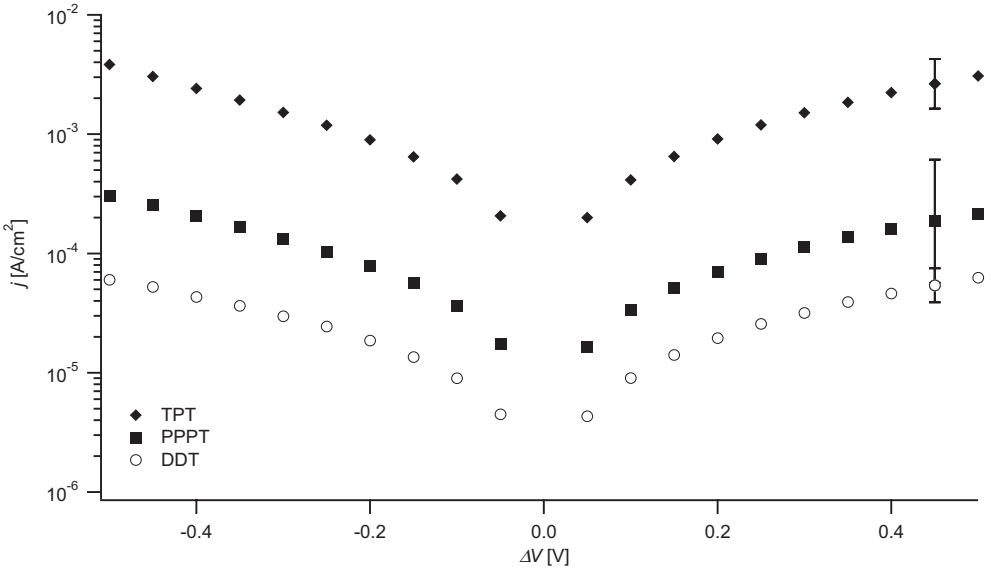

Figure 5. *I–V* curves measured across the Au–DDT//DDT–Hg, Au–PPPT//DDT–Hg and Au–TPT//DDT–Hg junctions. The error bars are shown for one voltage step only. They represent the standard deviation from the average values obtained from about 20 measurements for each type of junction.

© 2007 WILEY-VCH Verlag GmbH & Co. KGaA, Weinheim

ADVANCED FUNCTIONAL MATERIALS

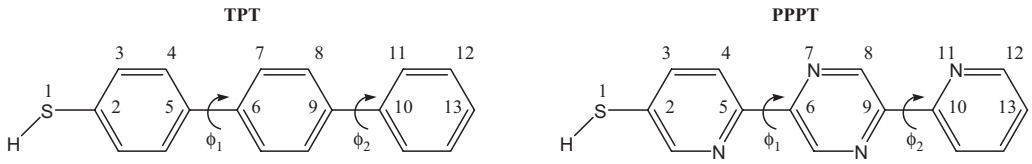

Figure 6. Chemical structures of TPT and PPPT. Atom numbering schemes for geometric analyses are also provided.

Table 3. Selected bond lengths (Å) and angles (°) for the neutral states of TPT and PPPT at the B3LYP/6-31G** level of theory.

	TPT			PPPT
	alternating	helical	planar	
S_1-C_2	1.787	1.787	1.786	1.779
C_2-C_3	1.401	1.401	1.400	1.401
C_3-C_4	1.391	1.391	1.390	1.388
C_4-C_5	1.405	1.405	1.408	1.403
C_5-C_6	1.483	1.483	1.487	1.480
C_6-C/N_7	1.405	1.405	1.407	1.345
C/N_7-C_8	1.391	1.391	1.389	1.331
C_8-C_9	1.405	1.405	1.407	1.406
C_9-C_{10}	1.484	1.484	1.490	1.484
C_{10}-C/N_{11}	1.405	1.405	1.408	1.346
C/N_{11}-C_{12}	1.394	1.394	1.393	1.335
C_{12}-C_{13}	1.396	1.396	1.395	1.396
φ_1	33.8	38.2	0.0	0.1
φ_2	–38.4	39.3	0.0	0.1
ΔE (kcal mol^{-1})	0.00	0.36	3.35	–

periments performed at room temperature (RT, approximately 0.6 kcal mol^{-1}). Specifically, it is known that oligophenylene–thiolates adopt, on average, a (near) planar conformation and pack in herringbone structures when self-assembled on Au.[63] Therefore, we scanned the potential energy surface for the rotation angle of the central phenyl ring, in both the alternating and helical conformations, as seen in Figure 7. Within the confines of RT, TPT in either the alternating or helical conformations could freely rotate between roughly 25–45°; because of the symmetry of the aryl segment of TPT, there was a corresponding rotation around 135–155°. It is worth noting that the most energetically destabilized conformation of TPT was at 90° where p-interaction stabilization was lost.

PPPT, in contrast, was severely limited in rotation about the central phenyl ring. At 180° (defined by the dihedral angle between the single nitrogen of the pyridine ring and the nearest-neighbor nitrogen on the pyrazine ring), hydrogen bonding interactions between the pyridine/pyrazine nitrogen atoms and hydrogen atoms on the neighboring aryl rings significantly stabilized the conformation; this stabilization was maintained for twists of approximately 10°. Beyond a torsion of 10°, there was a strong energetic destabilization of the molecule, as both the hydrogen-bonding and π-interaction stabilizations were lost. Furthermore, induced steric interactions (i.e., CH-HC) added to the energy destabilization as the twist approached 0°. As with TPT, the most energetically destabilized conformation was at 90°. HF/6-31G** simulations of these torsion potentials provided similar energy surfaces for both TPT and PPPT. We

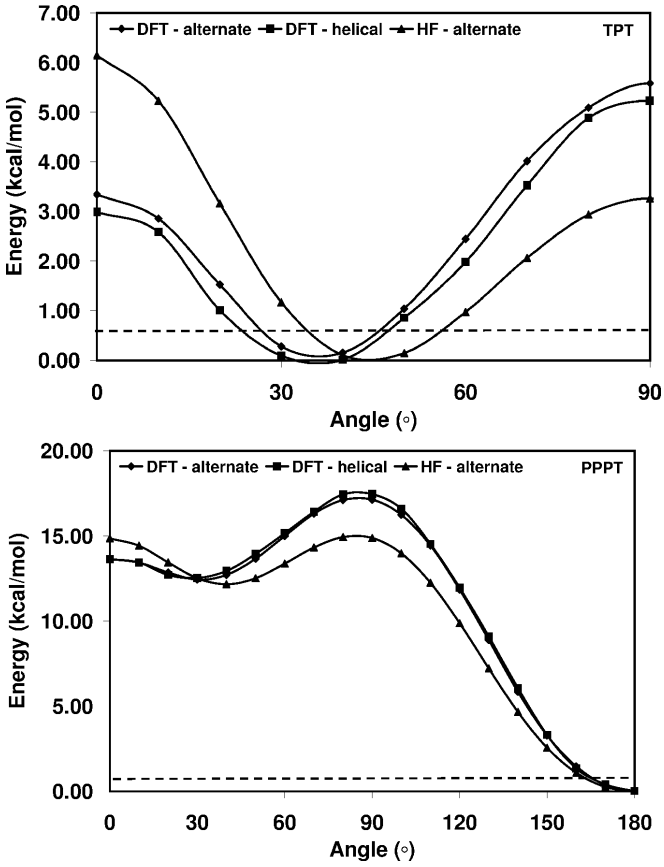

Figure 7. Potential energy surface for rotation about the central phenyl ring of TPT (top) and PPPT (bottom) at both the B3LYP/6-31G** and HF/6-31G** levels. The dashed bottom line represents energy at RT (0.6 kcal mol^{-1}).

also note that at a 0° conformation for PPPT, the nitrogen atoms of the pyridine-pyrazine pairs resided on the same side of the molecular structure. Such a structure provided the 2,2'-bipyridyl motif that could be utilized to incorporate metal ions into the molecular structure.

2.3.2. Electronic Structure

Energy eigenvalues for selected valence molecular orbitals of TPT and PPPT for various molecular conformations are listed in Table 4, whereas the respective pictorial representations of the surface densities are shown in Figures 8 and 9. For the optimized molecular conformation, the highest occupied molecular orbital (HOMO) for TPT (-5.61 eV) is located predominantly on the sulfur atom and the two adjacent phenyl

© 2007 WILEY-VCH Verlag GmbH & Co. KGaA, Weinheim

Table 4. Energy eigenvalues (eV) for selected valence molecular orbitals for various conformations of TPT and PPPT at the B3LYP/6-31G** level of theory.

	TPT			PPPT		
	opt.	0	90	opt.	0	90
LUMO+1	–0.30	–0.44	–0.16	–1.20	–1.14	–0.93
LUMO	–1.12	–1.39	–0.44	–2.04	–2.04	–1.42
HOMO	–5.61	–5.44	–5.93	–6.01	–6.04	–6.34
HOMO-1	–6.37	–6.39	–6.64	–6.53	–6.50	–6.64

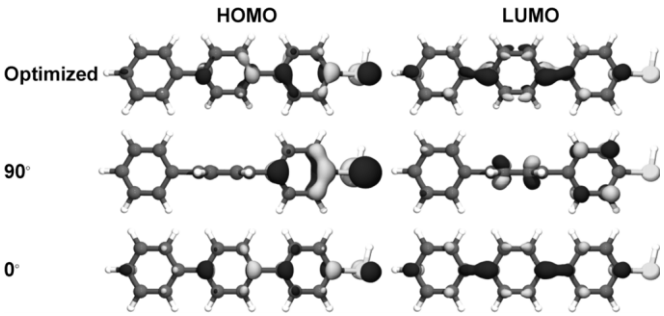

Figure 8. Pictorial representation of selected valence molecular orbitals of TPT at the B3LYP/6-31G** level of theory.

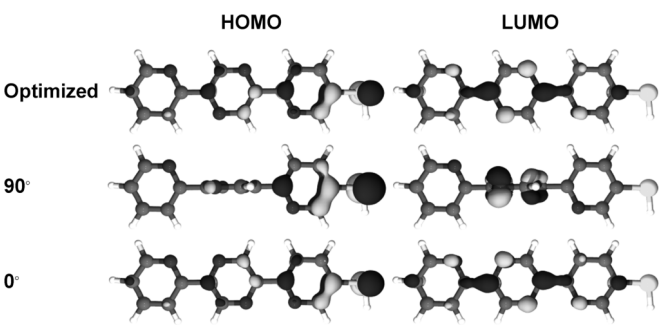

Figure 9. Pictorial representation of selected valence molecular orbitals of PPPT at the B3LYP/6-31G** level of theory.

rings, with little density on the outermost phenyl ring. In contrast, the lowest unoccupied molecular orbital (LUMO, –1.12 eV) is fully delocalized over the phenyl rings with a smaller density on the sulfur. Twisting the central phenyl ring to 90° fully localized the HOMO (–5.93 eV) on the sulfur and nearest-neighbor phenyl ring. Interestingly, the HOMO was energetically stabilized upon twisting the molecular structure; although the π-delocalization energy was lost, this gain in energy stabilization appeared to result from the lack of anti-bonding interaction between the phenyl rings. The LUMO was energetically destabilized (–0.44 eV) as it became localized on the two phenyl rings nearest the sulfur. Forcing TPT to be fully planar energetically destabilized the HOMO (–5.44 eV) while stabilizing the LUMO (–1.39 eV). The (de)stabilization effects were due to increased bonding and anti-bonding interactions in the HOMO and LUMO, respectively, between the phenyl rings.

The HOMO (-6.01 eV) and LUMO (-2.04 eV) of PPPT were energetically stabilized with respect to TPT. The optimized conformation for PPPT shares a similar wavefunction distribution for the HOMO (predominately on the sulfur atom and the two adjacent phenyl rings with little density on the furthest phenyl ring) and LUMO (delocalized over the phenyl rings with little-to-no density on the sulfur) with TPT. Similarly, the HOMO and LUMO wavefunction distribution for the 90° conformation was also similar to TPT.

2.3.3. Charge Distributions

Mulliken charge distributions at the B3LYP/6-31G** level of theory for TPT and PPPT are presented in Table 5. The charge distributions among the various TPT conformations did not change dramatically. The sulfur atom in PPPT was more electropositive that in TPT, a result that is in line with the XPS findings (see Section 2.1). The nitrogen atoms, as indicated by their highly negative Mulliken charges, act as strong electron-withdrawing agents in the aromatic backbone; this highly negative character of the nitrogen atoms helped to produce the stronger-than-expected hydrogen-bonding stabilization energy for this system. We also note that there was a significant redistribution of the charge character on the carbon atoms in PPPT versus TPT; the sum of the charges on the carbon atoms were more positive in PPPT than in TPT, in agreement with the XPS results.

Table 5. Mulliken charge distributions (arbitrary units) for TPT and PPPT at the B3LYP/6-31G** level of theory.

	TPT			PPPT
	alternating	helical	planar	
S_1	0.076	0.077	0.079	0.101
C_2	–0.087	–0.087	–0.084	–0.105
C_3	–0.007	–0.007	–0.012	0.041
C_4	–0.013	–0.011	–0.017	0.053
C_5	0.060	0.055	0.074	0.236
C_6	0.075	0.067	0.097	0.247
C/N_7	–0.037	–0.034	–0.050	–0.496
C_8	–0.034	–0.032	–0.047	0.235
C_9	0.067	0.064	0.093	0.243
C_{10}	0.063	0.062	0.083	0.245
C/N_{11}	–0.027	–0.027	–0.034	–0.505
C_{12}	–0.004	–0.004	–0.008	0.200
C_{13}	0.003	0.003	0.006	–0.003

3. Discussion

The XPS and NEXAFS data agreed remarkably well. SAMs of PPPT on both Au and Ag were well-ordered and densely packed, and the packing densities of the aromatic moieties in PPPT/Au and PPPT/Ag were found to be quite similar. Attachment to the substrate occurred via a thiolate linkage, whereas the pyridine-pyrazine backbone has an upward orientation.

© 2007 WILEY-VCH Verlag GmbH & Co. KGaA, Weinheim

Accordingly, the average tilt angles of the aromatic backbones in the PPPT/Au and PPPT/Ag structures were very close to each other, with a slightly smaller molecular inclination in PPPT/Au. This behavior is unusual because thiol-derived SAMs generally exhibit a larger molecular inclination on Au compared to Ag.[30,39,64] The average tilt angles of the aromatic backbones in PPPT/Au and PPPT/Ag were noticeably larger than the analogous values for the oligophenylene–thiolate SAMs of the same chain length on the same substrates. Whereas we found tilt angles of 32° and 35° for PPPT/Au and PPPT/Ag, values of 20° and 16° were obtained for TPT/Au and TPT/Ag, respectively.[30] Along with the smaller tilt in PPPT/Au compared to PPPT/Ag, this finding suggests that the incorporation of the nitrogen atoms into the phenyl rings distorted, to some extent, the molecular arrangement of the SAM constituents, which, in the case of aromatic SAMs, was mostly governed by the π–σ interaction between the adjacent molecular backbones.[44,56,63] For TPT SAMs, the π–σ interaction resulted in dense molecular packing with a herringbone arrangement of the SAM constituents[56] that was accompanied by a decrease in the molecular twist and subsequently resulted in an average planar conformation of the individual molecules.[63] Further, our XPS data indicate that an additional interaction related to the formation of hydrogen bonds between adjacent PPPT molecules occurred at most to a very limited extent. These differing intermolecular interactions in PPPT SAMs led to a lower packing density-approximately 80–85 % of that found for TPT SAMs.

With a thorough understanding of the properties of the PPPT SAMs, we can now explicitly focus on the issue of the dramatic reduction in conductance versus TPT. Considering the observed difference in the packing density of the PPPT and TPT SAMs, the fact that we obtained lower current densities-approximately one order of magnitude lower-for the thinner PPPT film suggests that the current flows through the individual molecules and not perpendicular across the SAM as a whole; for a "through-film" mechanism to be applicable, a higher current flow would be expected for the thinner film, which is an effect opposite to our observations for the PPPT and TPT films. This result is in accordance with a through-bond mechanism proposed for similar junctions.[5,8,25,65] Therefore, the lower packing density was not sufficient to explain the observed differences in current density. Within the Landauer limit for large gaps and constant self energies, current flow through organic films or tunneling junctions could be approximately written as

$$I(V) = \frac{2e}{\pi\hbar}\Gamma_1\Gamma_2\left(\frac{t^{2(N-1)}}{1-2N}\right)$$

$$\left(\left(\Phi_B + \frac{eV}{2}\right)^{1-2N} - \left(\Phi_B - \frac{eV}{2}\right)^{1-2N}\right) \qquad (2)$$

where N is the number of tunneling sites, t is the electronic coupling (transfer integral) between adjacent sites; $\Gamma_{1,2}$ are the coupling strengths between the molecule termini and metal electrodes; and Φ_B is the charge injection barrier from the electrode to the molecule.[66] The experimental XPS data and the calculated charge distributions indicate that the Au-S bond in PPPT was weakened versus TPT via a redistribution of molecular charge (i.e., withdrawal of negative charge by the incorporated nitrogen atoms)-a condition that also led to the observation of limited "self-cleaning" of the metal surface by PPPT versus oligophenylene–thiolate structures. Because of the weaker Au-S bond, we could expect $\Gamma_{1,2}$ to be smaller in PPPT versus TPT, an important factor in determining the conductance of a molecular junction.[5,18,65] However, we are not certain whether the observed small change in molecular electron density outweighs the effective tunneling barriers of the molecular spacers themselves.

According to the transport model, a second factor that can play a significant role is the injection barrier, Φ_B, which is the energetic difference between the metal work function Φ_{Au} and the ionization energy of the molecule (often roughly approximated as the HOMO (hole transport) or LUMO (electron transport) energy via Koopmans' theorem[67]). Figure 10 presents a pictorial representation of the energy level alignment of the HOMO and LUMO levels for PPPT and TPT as a function

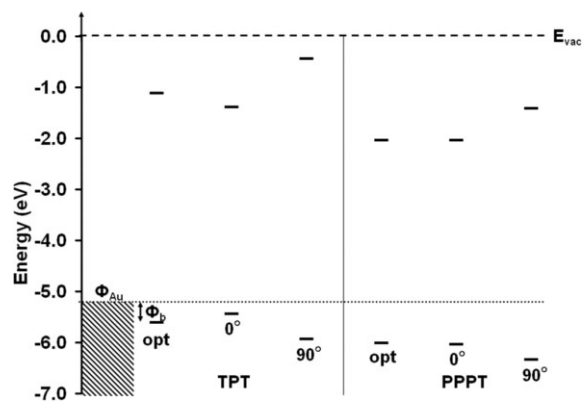

Figure 10. Energy level alignment for the HOMO and LUMO levels of PPPT and TPT as a function of geometric conformation with respect to Φ_{Au}. The molecular orbital energies were determined at the B3LYP/6-31G** level.

of geometric conformation with respect to Φ_{Au}. Computationally, we found that the HOMO and LUMO of PPPT are energetically stabilized versus TPT by approximately 0.6 eV for the planar geometry conformations. Assuming hole-type transport through the molecular conduction channels for these oligoarylene systems,[68–71] such energetic stabilization can hinder the hole injection process by making Φ_B larger for PPPT-the energy stabilization of the HOMO in PPPT increases the barrier for injection by moving the molecular level further away from the Au work function (with respect to TPT). As a check for the Koopmans' estimate, direct evaluation of the adiabatic [vertical] ionization potentials (6.83 eV [6.72 eV] for planar TPT and 7.43 eV [7.32 eV] for PPPT) also suggests an increased barrier for PPPT.

To determine how even modest differences in Φ_B can affect I–V characteristics, we utilized Equation 2 to evaluate current ratios of the two species, as seen in Figure 11. Assuming similar

 © 2007 WILEY-VCH Verlag GmbH & Co. KGaA, Weinheim

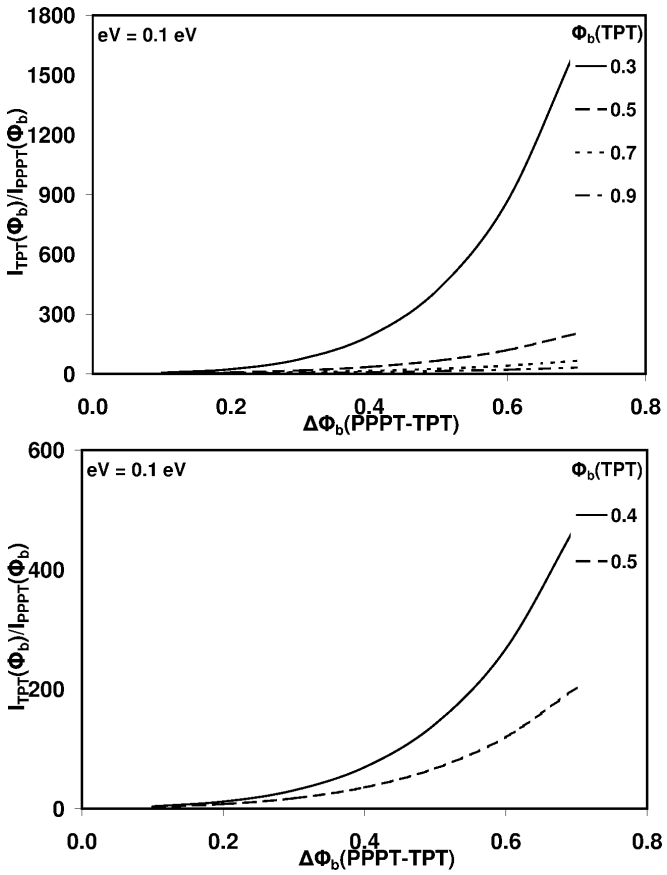

Figure 11. Ratio of the currents for TPT and PPPT as a function of Φ_B(TPT) for eV = 0.1 eV. N = 3 to account for the three rings in each molecular system.

electrode–molecule and electronic intersite couplings, setting $N = 3$ (to account for the three aryl rings in both PPPT and TPT) and collecting the constant terms, Equation 2 can be rewritten as

$$I(V) \propto \left(\Phi_B + \frac{eV}{2}\right)^{-5} - \left(\Phi_B - \frac{eV}{2}\right)^{-5} \tag{3}$$

Thus, the ratio of currents for the two molecular systems with respect to their injection barriers is

$$\frac{I_{TPT}\left(\Phi_B^{TPT}\right)}{I_{PPPT}\left(\Phi_B^{PPPT}\right)} \propto \frac{\left(\Phi_B^{TPT} + \frac{eV}{2}\right)^{-5} - \left(\Phi_B^{TPT} - \frac{eV}{2}\right)^{-5}}{\left(\Phi_B^{PPPT} + \frac{eV}{2}\right)^{-5} - \left(\Phi_B^{PPPT} - \frac{eV}{2}\right)^{-5}} \tag{4}$$

In the low-voltage limit, $I(\Phi_B) \propto eV \cdot \Phi_B^{-6}$, thus the ratio can be further simplified to

$$\frac{I_{TPT}\left(\Phi_B^{TPT}\right)}{I_{PPPT}\left(\Phi_B^{PPPT}\right)} \propto \left(\frac{\Phi_B^{PPPT}}{\Phi_B^{TPT}}\right)^6 \tag{5}$$

Fixing $\Phi_B{}^{\mathrm{TPT}}$, the current ratio increased dramatically at even 'small' differences in Φ_B (ca. 0.3–0.5 eV). Assuming a gold work function of 5.1 eV and using the HOMO energy for the planar TPT structure (-5.44 eV), $\Phi_B{}^{\mathrm{TPT}}$ is roughly on the order of 0.3–0.4 eV; noting that the HOMO energy difference (Δ_{HOMO}) between the planar TPT structure and PPPT was approximately 0.5–0.6 eV, the current ratio in this range was on the order of two orders of magnitude. Allowing for some geometric freedom in the twisting of the TPT structure, $\Phi_B{}^{\mathrm{TPT}}$ increased and Δ_{HOMO} decreased, as seen in Figure 10. If the increase in $\Phi_B{}^{\mathrm{TPT}}$ was approximately 0.2 eV and the decrease in Δ_{HOMO} was ca. 0.1 eV, the current ratio difference dropped to approximately one order of magnitude, a result well in line with the empirically derived *I–V* differences of TPT and PPPT. Note that as Φ_B of the reference molecular system increased, the current ratios were not so dramatically different as the injection barrier of the second molecule increased, indicating that there is some Φ_B above which a further increase did not significantly affect the current.

Apart from the parameters of the individual molecules, effects of the molecular environment can also be important.[25] As mentioned above, the local environment could affect the molecular conformation. In addition, it could influence such parameters as the electrostatic potential distribution across the molecule,[25,72,73] which may be of importance for molecular conductance in the tunneling regime. In general, such effects of the environment on the electrical properties of molecules have not been systematically studied and further work must be done.

4. Conclusion

We have analyzed the effects induced by the incorporation of nitrogen atoms into the backbone of aryl-based molecular wires by comparing the geometrical/organizational parameters, electronic structure, and electrical properties of a new heteroaromatic molecule, PPPT, and the structurally analogous TPT system. Both experimental data and theoretical calculations were used to interpret the different electrical properties of the two compounds.

The organizational parameters of PPPT and TPT SAMs on Au and Ag substrates, crucial for the interpretation of the electrical measurements, were obtained by XPS and NEXAFS spectroscopy. PPPT forms high-quality SAMs on both substrates but exhibits lower packing densities (by 15–20 %) and poorer orientational order than TPT films. Some of these differences can be attributed to the electronic effect of the nitrogen atoms, which results in a distortion of intermolecular interactions within the film and a weakening of the thiolate bond to the metal surface.

The conductance of PPPT is inferior to the value for a TPT SAM: at the same bias voltage, the current density across the PPPT films was an order of magnitude lower. The lower packing density and conductance in PPPT point to the assignment of a through-bond mechanism for charge transport in these molecular films.

Theoretical calculations with DFT were used to probe the geometric structure, valence molecular orbitals, and charge dis-

© 2007 WILEY-VCH Verlag GmbH & Co. KGaA, Weinheim

ADVANCED FUNCTIONAL MATERIALS

tributions for the PPPT and TPT molecules. The relative positions of the calculated molecular orbital energies (ionization energies) suggest a larger energy barrier for a hole transfer tunneling mechanism for PPPT with respect to TPT; indeed, it was shown that small differences in injection barriers can have dramatic consequences for comparative currents. Using simple models for the tunneling conductance, we calculated a conduction ratio very close to one order of magnitude, in agreement with experiment. It is, however, important to stress that not only the difference in the injection barrier but also the different geometrical parameters of the PPPT film (as compared to TPT) and a weakening of the thiolate bond to the metal surface contributes to the observed lower conductance of the PPPT SAM as well.

The results presented here underline the possible mechanistic complications for molecular conductance in densely packed monomolecular films. The experimental data and theoretical calculations reveals how electrical properties can be discussed in terms of precise molecular orientation and density, conformation, bonding, and local environment in the films, in addition to molecular electronic structure. We believe that the field of molecular electronics could benefit from taking into account all of these parameters and their relative contributions.

5. Experimental

5.1. Synthesis of PPPT

The synthesis of PPPT is illustrated in Scheme 1.

*2-Bromo-5-(methylsulfanyl)pyridine (**1**)*: To a solution of 2,5-dibromopyridine (21.72 g, 91.7 mmol) in 330 mL anhydrous diethyl ether under argon at –78 °C was added 44 mL *n*-butyl lithium (2.5 M in hexane, 110 mmol) [74]. The solution was stirred at –78 °C for 40 min, at which time 16.5 mL methyl disulfide (17.28 g, 183.4 mmol) was added. The solution was warmed to room temperature, and 300 mL H_2O was added. The two layers were separated, and the aqueous layer was washed with 300 mL ether. The combined organic layers were dried over Na_2SO_4. After removal of the solvent, the crude product was chromatographed on silica gel using 30 % CH_2Cl_2 in hexanes as the eluant. Recrystallization from hexanes gave **1** as white needles (13.08 g, 69 %). ^{1}H NMR (300 MHz, $CDCl_3$, d): 8.26 (dd, J = 2.42 Hz, 0.67 Hz, 1H), 7.45 (dd, J = 8.34 Hz, 2.52 Hz, 1H), 7.40 (dd, J = 8.33 Hz. 0.71 Hz, 1H), 2.53 ppm (s, 3H).

*5-[5-(Methylsulfanyl)pyridin-2-yl]pyrazin-2-amine (**2**)*: **1** (6.67 g, 32.0 mmol), 5-(trimethylstannyl)aminopyrazine [75] (7.00 g, 27.1 mmol), and tetrakis(triphenylphosphine) palladium(0) (1.57 g, 1.36 mmol) were dissolved in 270 mL toluene, and the mixture was heated under argon at 110 °C. The mixture was stirred for 24 h, and the toluene was evaporated. The residue was chromatographed on silica gel using a 50–100 % gradient elution (ethyl acetate in hexanes). **2** was isolated as a yellow powder (4.45 g, 75 %). ^{1}H NMR (300MHz, $CDCl_3$, d): 9.10 (d, J = 1.35 Hz, 1H), 8.60 (d, J = 2.26 Hz, 1H), 8.16 (d, J = 8.43 Hz, 1H), 8.12 (d, J = 1.40 Hz, 1H), 7.75 (dd, J = 8.43 Hz, 2.44 Hz, 1H), 4.91 (s, broad, 2H), 2.65 ppm (s, 3H).

*2-Iodo-5-[5-(methylsulfanyl)pyridin-2-yl]pyrazine (**3**)*: **2** (1.99 g, 9.13 mmol), iodine chips (4.63 g, 18.26 mmol), and NaI (5.47 g, 36.5 mmol) were dissolved in 100 mL anhydrous benzene. The mixture was cooled to 0 °C, and isoamyl nitrite (2.14 g, 18.3 mmol) was added dropwise. The mixture was heated in a sealed thick-wall tube at 80 °C. After 24 h, the mixture was cooled to room temperature, and the tube was opened carefully to release the pressure inside. The mixture was poured into 50 mL H_2O. Under vigorous stirring, solid $Na_2S_2O_3{\cdot}5H_2O$ was added until the color turned from dark purple to yellow. The two layers were separated, and the aqueous layer was extracted with CH_2Cl_2 repeatedly. The combined organic layers were washed with brine and H_2O and then dried over Na_2SO_4. After removal of the solvent, the crude product was chromatographed on silica gel using CH_2Cl_2 as the eluant. **3** was isolated as a yellow powder (1.77 g, 59 %). ^{1}H NMR (300MHz, $CDCl_3$, d): 9.37 (d, J = 1.43 Hz, 1H), 8.84 (d, J = 1.41 Hz, 1H), 8.56 (d, J = 2.11 Hz, 1H), 8.25 (d, J = 8.29 Hz, 1H), 7.68 (dd, J = 8.36 Hz, 2.41 Hz, 1H), 2.60 ppm (s, 3H).

*2-Iodo-5-[5-(methylsulfinyl)pyridin-2-yl]pyrazine (**4**)*: **3** (1.74 g, 5.30 mmol) was dissolved in 200 ml CH_2Cl_2, and the solution was cooled to -20 °C. Under vigorous stirring, a solution of *m*-chloroperbenzoic acid (*m*CPBA) (1.31 g of a 70–75 % water suspension) in 50ml CH_2Cl_2 was added dropwise over 1 h. The solution was stirred at 0 °C for an additional hour. To this mixture $Ca(OH)_2$ (0.80 g) and Na_2SO_4 were added, and stirring was continued at room temperature for another hour. After filtering, the solution was concentrated. **4** was obtained as a yellow powder (1.69 g, 92 %). It was ready for the next reaction step without further purification. ^{1}H NMR (300MHz, $CDCl_3$, d): 9.46 (d, J = 1.50 Hz, 1H), 8.91 (d, J = 1.50 Hz, 1H), 8.8 (dd, J = 2.13 Hz, 0.06 Hz, 1H), 8.56 (d, J = 8.40 Hz, 0.06 Hz, 1H), 8.22 (dd, J = 8.17 Hz, 2.20 Hz, 1H), 2.89 ppm (s, 3H).

*2-[5-(Methylsulfinyl)pyridin-2-yl]-5-pyridin-2-ylpyrazine (**5**)*: **4** (1.252 g, 3.63 mmol), 2-(trimethylstannyl)pyridine (1.316 g, 3.19 mmol), and

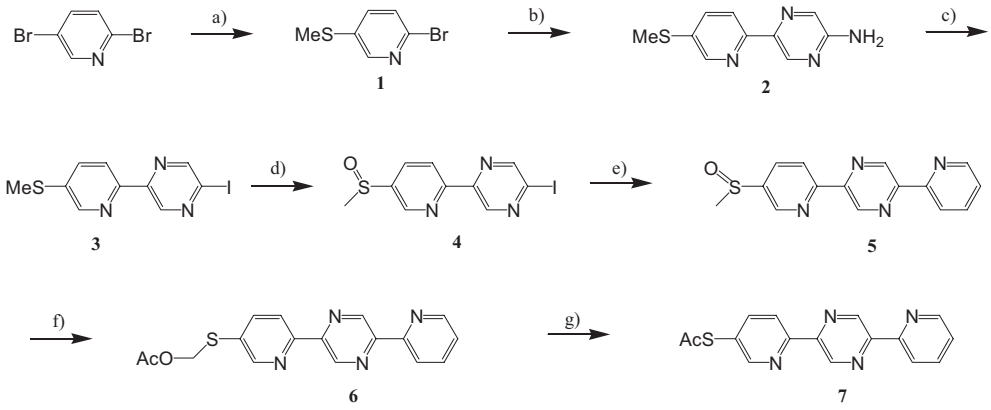

Scheme 1. Synthesis of the PPPT precursor (7, acetyl-protected PPPT). a) 1. *n*BuLi, -78 °C, Et_2O; 2. MeSSMe; b) 5-(Trimethylstannyl)aminopyrazine, $Pd(PPh_3)_4$, toluene; c) Isoamyl nitrite, I_2, NaI, benzene: d) *m*CPBA, CH_2Cl_2; e) 2-(Trimethylstannyl)pyridine, $Pd(PPh_3)_4$, dioxane; f) 1. Ac_2O; 2. $NaHCO_3$; g) 1. HCl/MeOH; 2. CH_3COCl, pyridine.

© 2007 WILEY-VCH Verlag GmbH & Co. KGaA, Weinheim

tetrakis(triphenylphosphine)palladium(0) (0.210 g, 0.18 mmol) were dissolved in 80 mL anhydrous dioxane. The mixture was heated at 100 °C under argon for 24 h, and then the dioxane was evaporated. The residue was chromatographed on silica gel using a 0–10 % gradient elution (methanol in CH_2Cl_2). **5** was isolated as a yellow powder (0.667 g, 63 %). ^{1}H NMR (300 MHz, $CDCl_3$, d): 9.72 (s, 2H), 8.92 (dd, J = 2.19 Hz, 0.45 Hz, 1H), 8.78 (ddd, J = 4.96 Hz 1.48 Hz, 0.74 Hz, 1H), 8.67 (dd, J = 8.28 Hz, 0.47 Hz, 1H), 8.48 (dd, J = 7.94 Hz, 0.84 Hz, 1H), 8.24 (dd, J = 8.30 Hz, 2.27 Hz, 1H), 7.91 (dt, J = 1.78 Hz, 7.70 Hz, 1H), 7.42 (ddd, J = 7.54 Hz, 4.80 Hz, 1.12 Hz, 1H), 2.90 ppm (s, 3H).

1-([6-(5-Pyridin-2-ylpyrazin-2-yl)pyridin-3-yl]sulfanyl)acetone (***6***): **5** (0.3411 g, 1.15 mmol) and *p*-toluenesulfonic acid (0.140 g) were dissolved in acetic anhydride (27 mL). The solution was heated under argon at 140 °C for 1 h and then cooled to room temperature and poured into a 100 mL saturated $NaHCO_3$ solution. Under vigorously stirring, solid $NaHCO_3$ was added slowly until the solution was slightly basic. The solution was stirred for an additional hour and then extracted with CH_2Cl_2 repeatedly. The combined organic layers were washed with saturated $NaHCO_3$ solution and then dried over Na_2SO_4. After removal of the solvent, the residue was chromatographed on silica gel using 3 % methanol in CH_2Cl_2 as the eluant. **6** was isolated as a light yellow powder (0.310 g, 89 %). ^{1}H NMR (300 MHz, $CDCl_3$, d): 9.68 (d, J = 1.30 Hz, 1H), 9.66 (d, J = 1.16 Hz, 1H), 8.81 (d, J = 2.17 Hz, 1H), 8.77 (d, J = 4.16 Hz, 1H), 8.48-8.43 (m, 2H), 87.96 (dd, J = 8.29 Hz, 2.33 Hz, 1H), 7.90 (dt, J = 1.79 Hz, 7.74 Hz, 1H), 7.42 (ddd, J = 7.53 Hz, 4.73 Hz, 1.04 Hz, 1H), 5.49 (s, 2H), 2.18 ppm (s, 3H).

*S-[6-(5-Pyridin-2-ylpyrazin-2-yl)pyridin-3-yl] ethanethioate (**7**)*: **6** (0.290 g, 0.86 mmol) was dissolved in 118 mL MeOH. To this solution was added 11.8 mL concentrated HCl dropwise under argon. The solution was heated at 75 °C for 3 h. The solvent was removed, and the residue was dissolved in 50 mL CH_2Cl_2. The solution was washed with a saturated $NaHCO_3$ solution repeatedly until the aqueous layer was basic. The organic layer was dried over Na_2SO_4, and 4.4 mL pyridine (4.30 g, 54 mmol) was added. This mixture was cooled to 0 °C, and 3.9 mL acetic chloride (4.30 g, 54 mmol) was added dropwise under argon. The mixture was stirred at 0 °C for 10 min and then warmed to room temperature. After 2 h, 50 mL H_2O was added. The two layers were separated, and the aqueous layer was washed with CH_2Cl_2 repeatedly. Combined organic layers were washed with brine and water and then dried over Na_2SO_4. After solvent removal, the crude product was recrystallized from ethyl acetate to give pure **7** as a yellow powder (0.117 mg, 44 %). ^{1}H NMR (300 MHz, $CDCl_3$, d): 9.71 (s, 2H), 8.78 (d, J = 4.37 Hz, 1H), 8.70 (d, J = 1.78 Hz, 21H), 8.53 (d, J = 8.22 Hz, 1H), 8.48 (d, J = 7.97 Hz, 1H), 7.94–7.89 (m, 2H), 7.41 (ddd, J = 7.5 Hz, 4.8 Hz, 0.9 Hz, 1H), 2.55 ppm (s, 3H); ^{13}C NMR (300MHz, $CDCl_3$, d): 192.71, 154.99, 154.42, 153.97, 151.02, 150.15, 149.75, 143.20, 142.58, 142.50, 137.67, 126.64, 124.88, 122.23 (likely more than one carbon atom because of its intensity), 30.854 ppm; HRMS (FAB, m/z): $[M + H]^+$ calcd for $C_{16}H_{12}N_4OS$, 308.07; found, 309.08.

5.2. Monolayer Preparation

Gold and silver substrates were prepared by thermal evaporation of 200 nm of gold (30 nm of gold for *I–V* measurements) or 100 nm of silver, 99.99 % purity, onto mica sheets or polished 3 inch single-crystal silicon (100) wafers (Silicon Sense) precoated with a 5 nm titanium adhesion layer. Such evaporated films are standard substrates for thiol-derivatized SAMs: they are polycrystalline with terrace sizes of several hundreds of nanometers (mica) or grain sizes of 20–50 nm (Si) and a predominant (111) orientation [76]. The PPPT SAMs were formed by immersion of freshly prepared substrates into a 0.02 or 0.3 mM solution of the PPPT precursor (**7**, acetyl-protected PPPT) in absolute ethanol at room temperature for 24 h. A drop of NH_4OH was added to the solution for deprotection. The TPT SAMs were formed by immersion of freshly prepared substrates into a 0.3 mM solution of TPT in absolute ethanol at room temperature for 24 h. The DDT SAMs were prepared according to the same protocol. After immersion, the samples were carefully rinsed with pure ethanol, blown dry with argon, and used immediately for *I–V* characterization. Samples to be analyzed at the synchrotron facility were stored for several days in argon-filled glass containers until characterization.

5.3. XPS and NEXAFS Spectroscopy

The SAMs were characterized by XPS and NEXAFS spectroscopy using a multitechnique ultrahigh vacuum (UHV) experimental station attached to the HE-SGM beamline at the German synchrotron radiation facility BESSY II in Berlin. The measurements were performed at room temperature under UHV conditions (base pressure better than 1.5×10^{-9} Torr, 1 Torr = 133.32 Pa). The spectra acquisition time was selected such that no noticeable damage by the primary X-rays occurred during the measurements [32-35].

XPS measurements were performed with a VG CLAM 2 spectrometer in normal emission geometry. The photon energy was varied from 400 to 660 eV, with an energy resolution of approximately 0.40 eV. The BE scale was referenced to the Au $4f_{7/2}$ peak at 84.0 eV [77]. For each sample, a survey scan and C 1s, N 1s, S 2p, O 1s, and Au 4f or Ag 3d multiplex scans were collected. The spectra were normalized to the photon flux and fitted by using a Shirley-type background [78] and symmetric Voigt functions [79] with a Gauss/Lorenz ratio of 4:1. To fit the S $2p_{3/2,1/2}$ doublet, we used a pair of such peaks with the same full-width at half maximum (FWHM), a standard [77] spin-orbit splitting of ca. 1.2 eV (verified by fit), and a branching ratio of 2 ($2p_{3/2}/2p_{1/2}$).

NEXAFS measurements were carried out at the C and N K-edges in the partial electron yield acquisition mode with retarding voltages of –150 and –300 V, respectively. Linear polarized synchrotron light with a polarization factor of ca. 82 % was used. The energy resolution was approximately 0.40 eV. The incidence angle of the synchrotron light was varied from 90° (**E**-vector in surface plane) to 20° (**E**-vector near the surface normal) in steps of 10°–20° to monitor the orientational order within the films. The raw NEXAFS spectra were normalized to the incident photon flux through division by a spectrum from a clean, freshly sputtered gold sample; in the case of the SAM/Ag, a spectrum of clean silver was subtracted from the raw spectrum of a SAM sample before the normalization [30,48]. Note that this procedure did not affect the resonance structure of the spectra but just corrected for the difference in the electron yield between gold and silver in the given photon energy range, which made comparison of the spectra for samples on Au and Ag more straightforward. The photon energy scale was referenced to the pronounced π_1* resonance of highly oriented pyrolitic graphite at 285.35 eV [80].

5.4. *I–V* Measurements

I–V measurements were performed on junctions incorporating PPPT, TPT, or DDT SAMs in a Au–X//DDT–Hg arrangement (X = PPPT, TPT, DDT). Junction assembly began by covering the gold electrodes with the respective target SAM. The mercury electrodes were prepared in situ by extruding a drop of liquid mercury from a glass capillary and exposing it to an aerated solution of 10 mM dodecanethiol in ethanol for 1 min. The mercury drop was removed from the thiol solution and rinsed with ethanol and hexadecane. The SAM-coated gold electrode immersed in hexadecane and the SAM-coated mercury drop were brought into contact by using a micromanipulator. The contact area was monitored by a camera through the transparent gold film and evaluated under 50-fold magnification to about 0.1 mm^2. The applied voltage was varied between –0.5 V and +0.5 V in steps of 0.05 V, and the current was measured with a 6430 Keithley Sub-Femtoamp Sourcemeter. Electrical measurements for each sample were performed two times at ten different locations; for each location, a new Hg drop was extruded from the capillary and coated with the dodecanethiol SAM before the next measurements. A detailed description of the experimental setup can be found elsewhere [81].

5.5. Computational Methodology

Geometry optimizations for the gas-phase neutral, radical-anion, and radical-cation states of TPT and PPPT were carried out at the DFT

© 2007 WILEY-VCH Verlag GmbH & Co. KGaA, Weinheim

level using the B3LYP functionals [82-84]; detailed information pertaining to the radical-ion states can be found in the Supporting Information. The optimizations were started from two conformations related to the twisting of the aryl groups: alternating and helical (see Fig. 12). Potential energy surfaces for twisting about the central aryl ring were generated at both the DFT and Hartree-Fock (HF) levels.

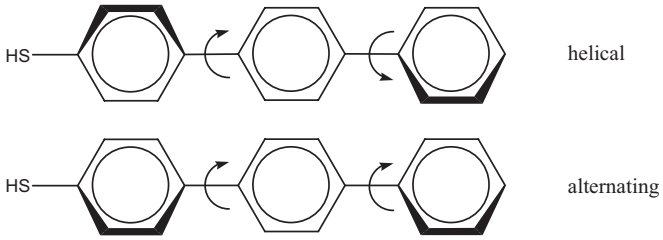

Figure 12. Representation of the alternating and helical molecular structures for TPT and PPPT.

All calculations utilized a 6-31G** split valence plus a double polarization basis set and were carried out with QChem (version 2.1) [85].

Received: April 20, 2007
Revised: June 28, 2007
Published online: November 14, 2007

[1] *Lecture Notes in Physics: Introducing Molecular Electronics*, Vol. 680 (Eds: G. Cuniberti, G. Fagas, K. Richter), Springer, Heidelberg **2005**.
[2] C. Joachim, M. A. Ratner, *Proc. Nat. Acad. Sci. USA* **2005**, *102*, 8801.
[3] X. Guo, J. P. Small, J. E. Klare, Y. Wang, M. S. Purewal, I. W. Tam, B. H. Hong, R. Caldwell, L. Huang, S. O'Brien, J. Yan, R. Breslow, S. J. Wind, J. Hone, P. Kim, C. Nuckolls, *Science* **2006**, *311*, 356.
[4] F. Anariba, J. K. Steach, R. L. McCreery, *J. Phys. Chem. B* **2005**, *109*, 11 163.
[5] V. B. Engelkes, J. M. Beebe, C. D. Frisbie, *J. Am. Chem. Soc.* **2004**, *126*, 14 287.
[6] A. Nitzan, M. A. Ratner, *Science* **2003**, *300*, 1384.
[7] D. M. Adams, L. Brus, C. E. D. Chidsey, S. Creager, C. Creutz, C. R. Kagan, P. V. Kamat, M. Lieberman, S. Lindsay, R. A. Marcus, R. M. Metzger, M. E. Michel-Beyerle, J. R. Miller, M. D. Newton, D. R. Rolison, O. Sankey, K. S. Schanze, J. Yardley, X. Zhu, *J. Phys. Chem. B* **2003**, *107*, 6668.
[8] D. J. Wold, R. Haag, M. A. Rampi, C. D. Frisbie, *J. Phys. Chem. B* **2002**, *106*, 2813.
[9] J. van Ruitenbeek, E. Scheer, H. B. Weber, in *Lecture Notes in Physics: Introducing Molecular Electronics*, Vol. 680 (Eds: G. Cuniberti, G. Fagas, K. Richter), Springer, Heidelberg **2005**, pp 253-274.
[10] B. Xu, X. Xiao, X. Yang, L. Zang, N. Tao, *J. Am. Chem. Soc.* **2005**, *127*, 2386.
[11] Y. Selzer, M. A. Cabassi, T. S. Mayer, D. L. Allara, *J. Am. Chem. Soc.* **2004**, *126*, 4052.
[12] Y. Selzer, M. A. Cabassi, T. S. Mayer, D. L. Allara, *Nanotechnology* **2004**, *15*, S483.
[13] J. Park, A. N. Pasupathy, J. I. Goldsmith, C. Chang, Y. Yaish, J. R. Petta, M. Rinkoski, J. P. Sethna, H. D. Abruna, P. L. McEuen, D. C. Ralph, *Nature* **2002**, *417*, 722.
[14] H. Park, J. Park, A. K. L. Kim, E. H. Anderson, P. A. Alivisatos, P. L. McEuen, *Nature* **2000**, *407*, 57.
[15] H. B. Akkerman, P. W. M. Blom, D. M. de Leeuw, B. de Boer, *Nature* **2006**, *441*, 69.
[16] A. M. Moore, A. A. Dameron, B. A. Mantooth, R. K. Smith, D. J. Fuchs, J. W. Ciszek, F. Maya, Y. Yao, J. M. Tour, P. S. Weiss, *J. Am. Chem. Soc.* **2006**, *128*, 1959.
[17] P. A. Lewis, C. E. Inman, F. Maya, J. M. Tour, J. E. Hutchison, P. S. Weiss, *J. Am. Chem. Soc.* **2005**, *127*, 17 421.
[18] F. R. F. Fan, Y. Yao, L. Cai, L. Cheng, J. M. Tour, A. J. Bard, *J. Am. Chem. Soc.* **2004**, *126*, 4035.
[19] C. D. Zangmeister, S. W. Robey, R. D. van Zee, J. G. Kushmerick, J. Naciri, Y. Yao, J. M. Tour, B. Varughese, B. Xu, J. E. Reutt-Robey, *J. Phys. Chem. B* **2006**, *110*, 17 138.
[20] L. T. Cai, H. Skulason, J. G. Kushmerick, K. S. Pollack, J. Naciri, R. Shashidhar, D. L. Allara, T. E. Mallouk, T. S Mayer, *J. Phys. Chem. B* **2004**, *108*, 2827.
[21] J. K. N. Mbindyo, T. E. Mallouk, J. B. Mattzela, I. Kratochvilova, B. Razavi, T. N. Jackson, T. S. Mayer, *J. Am. Chem. Soc.* **2002**, *124*, 4020.
[22] J. G. Kushmerick, D. B. Holt, J. C. Yang, J. Naciri, M. H. Moore, R. Shashidhar, *Phys. Rev. Lett.* **2002**, *89*, 086 802/1.
[23] Y. Selzer, A. Salomon, D. Cahen, *J. Phys. Chem. B* **2002**, *106*, 10 432.
[24] Y. Selzer, A. Salomon, D. Cahen, *J. Am. Chem. Soc.* **2002**, *124*, 2886.
[25] Y. Selzer, L. Cai, M. A. Cabassi, Y. Yao, J. M. Tour, T. S. Mayer, D. L. Allara, *Nano Lett.* **2005**, *5*, 61.
[26] M. Duati, C. Grave, N. Tcbeborateva, J. Wu, K. Müllen, A. Shaporenko, M. Zharnikov, J. K. Kriebel, G. M. Whitesides, M. A. Rampi, *Adv. Mater.* **2006**, *18*, 329.
[27] J. D. Monnell, J. J. Stapleton, S. M. Dirk, W. A. Reinerth, J. M. Tour, D. L. Allara, P. S. Weiss, *J. Phys. Chem. B* **2005**, *109*, 20 343.
[28] A. Shaporenko, A. Terfort, M. Grunze, M. Zharnikov, *J. Electron Spectrosc. Relat. Phenom.* **2006**, *151*, 45.
[29] A. Shaporenko, M. Brunnbauer, A. Terfort, M. Grunze, M. Zharnikov, *J. Phys. Chem. B* **2004**, *108*, 14 462.
[30] S. Frey, V. Stadler, K. Heister, W. Eck, M. Zharnikov, M. Grunze, B. Zeysing, A. Terfort, *Langmuir* **2001**, *17*, 2408.
[31] R. E. Holmlin, R. F. Ismagilov, R. Haag, V. Mujica, M. A. Ratner, M. A. Rampi, G. M. Whitesides, *Angew. Chem. Int. Ed.* **2001**, *40*, 2316.
[32] M. Zharnikov, M. Grunze, *J. Vac. Sci. Technol. B* **2002**, *20*, 1793.
[33] K. Heister, M. Zharnikov, M. Grunze, L. S. O. Johansson, A. Ulman, *Langmuir* **2001**, *17*, 8.
[34] M. Wirde, U. Gelius, T. Dunbar, D. L. Allara, *Nucl. Instrum. Methods Phys. Res. B* **1997**, *131*, 245.
[35] B. Jäger, H. Schürmann, H. U. Müller, H.-J. Himmel, M. Neumann, M. Grunze, C. Wöll, *Z. Phys. Chem.* **1997**, *202*, 263.
[36] J. J. Yeh, I. Lindau, *At. Data Nucl. Data Tables* **1985**, *32*, 1.
[37] S. M. Goldberg, C. S. Fadley, S. Kono, *J. Electron Spectrosc. Relat. Phenom.* **1981**, *21*, 285.
[38] I. M. Band, Y. I. Kharitonov, I. Yu, M. B. Trzhaskovskaya, *At. Data Nucl. Data Tables* **1979**, *23*, 443.
[39] M. Zharnikov, M. Grunze, *J. Phys.: Condens. Matter* **2001**, *13*, 11 333.
[40] K. Heister, M. Zharnikov, M. Grunze, L. S. O. Johansson, *J. Phys Chem. B* **2001**, *105*, 4058.
[41] P. E. Laibinis, G. M. Whitesides, D. L. Allara, Y.-T. Tao, A. N. Parikh, R. G. Nuzzo, *J. Am. Chem. Soc.* **1991**, *113*, 7152.
[42] Y. Zubavichus, M. Zharnikov, Y. Yang, O. Fuchs, C. Heske, E. Umbach, A. Ulman, M. Grunze, *Langmuir* **2004**, *20*, 11 022.
[43] X. Zhou, S. H. Goh, S. Y. Lee, K. L. Tan, *Appl. Surf. Sci.* **1998**, *126*, 141.
[44] A. Ulman, *Acc. Chem. Res.* **2001**, *34*, 855.
[45] J. F. Kang, A. Ulman, S. Liao, R. Jordan, *Langmuir* **1999**, *15*, 2095.
[46] C. L. A. Lamont, J. Wilkes, *Langmuir* **1999**, *15*, 2037.
[47] J. Thome, M. Himmelhaus, M. Zharnikov, M. Grunze, *Langmuir* **1998**, *14*, 7435.
[48] M. Zharnikov, S. Frey, K. Heister, M. Grunze, *Langmuir* **2000**, *16*, 2697.
[49] H. Kondoh, M. Iwasaki, T. Shimada, K. Amemiya, T. Yokoyama, T. Ohta, M. Shimomura, S. Kono, *Phys. Rev. Lett.* **2003**, *90*, 066 102/1.
[50] J. Stöhr, *NEXAFS Spectroscopy*, Springer Series in Surface Science 25, Springer-Verlag, Berlin **1992**.
[51] J. L. Solomon, R. J. Madix, J. Stöhr, *Surf. Sci.* **1991**, *255*, 12.

© 2007 WILEY-VCH Verlag GmbH & Co. KGaA, Weinheim

[52] T. Yokoyama, K. Seki, I. Morisada, K. Edamatsu, T. Ohta, *Phys. Scripta* **1990**, *41*, 189.
[53] J. Horsley, J. Stöhr, A. P. Hitchcock, D. C. Newbury, A. L. Johnson, F. Sette, *J. Chem. Phys.* **1985**, *83*, 6099.
[54] S. Aminpirooz, L. Becker, B. Hillert, J. Haase, *Surf. Sci.* **1991**, *244*, L152.
[55] R. Dudde, K. H. Frank, E. E. Koch, *J. Electron Spectrosc. Relat. Phenom.* **1988**, *47*, 245.
[56] H.-J. Himmel, A. Terfort, C. Wöll, *J. Am. Chem. Soc.* **1998**, *120*, 12 069.
[57] M. Bader, J. Haase, K.-H. Frank, A. Puschmann, A. Otto, *Phys. Rev. Lett.* **1986**, *56*, 1921.
[58] M. Bader, J. Haase, K.-H. Frank, K. Ocal, A. Puschmann, A. Otto, *J. de Physique* **1986**, *C8*, C8.
[59] A. Shaporenko, K. Adlkofer, L. S. O. Johansson, M. Tanaka, M. Zharnikov, *Langmuir* **2003**, *19*, 4992.
[60] M. Zharnikov, A. Küller, A. Shaporenko, E. Schmidt, W. Eck, *Langmuir* **2003**, *19*, 4682.
[61] W. Azzam, P. Cyganik, G. Witte, M. Buck, C. Wöll, *Langmuir* **2003**, *19*, 8262.
[62] S.-C. Chang, I. Chao, Y.-T. Tao, *J. Am. Chem. Soc.* **1994**, *116*, 6792.
[63] A. Shaporenko, M. Elbing, A. Blaszczyk, C. von Hänisch, M. Mayor, M. Zharnikov, *J. Phys. Chem. B* **2006**, *110*, 4307.
[64] A. Ulman, *Chem. Rev.* **1996**, *96*, 1533.
[65] J. M. Beebe, V. B. Engelkes, L. L. Miller, C. D. Frisbie, *J. Am. Chem. Soc.* **2002**, *124*, 11 268.
[66] V. Mujica, M. A. Ratner, *Chem. Phys.* **2001,** *264*, 365.
[67] T. Koopmans, *Physica* **1933,** *1*, 104.
[68] Y. Xue, M. A. Ratner, *Phys. Rev. B* **2003,** *68*, 115 406/01.
[69] A. Nitzan, *Annu. Rev. Phys. Chem.* **2001**, *52*, 681.
[70] C. G. Cameron, T. J. Pittman, P. G. Pickup, *J. Phys. Chem. B* **2001**, *105*, 8838.
[71] C. Joachim, J. K. Gimzewski, A. Aviram, *Nature* **2000,** *408*, 541.
[72] G. Heimel, L. Romaner, J.-L. Brédas, E. Zojer, *Surf. Sci.* **2006**, *600*, 4548.
[73] G. Heimel, L. Romaner, E. Zojer, J.-L. Brédas, *Nano Lett.* **2007**, *7*, 932.
[74] Under these conditions (high concentration, coordinating solvent and –78 °C), lithium-halogen exchange takes place at the 5′ position. X. Wang, P. Rabbat, P. O'Shea, R. Tillyer, E. J. J. Grabowski, P. J. Reider, *Tetrahedron Lett.* **2000**, *41*, 4335.
[75] U. Ziener, E. Breuning, J. M. Lehn, E. Wegelius, K. Rissanen, G. Baum, D. Fenske, G. Vaughan, *Chem. Eur. J.* **2000**, *6*, 4132.
[76] F. Köhn, *Diploma Thesis*, Universität Heidelberg, Heidelberg **1998**.
[77] J. F. Moulder, W. E. Stickle, P. E. Sobol, K. D. Bomben, in *Handbook of X-ray Photoelectron Spectroscopy* (Ed: J. Chastian), Perkin-Elmer Corp., Eden Prairie, MN **1979**.
[78] D. A. Shirley, *Phys. Rev. B* **1972**, *5*, 4709.
[79] G. K. Wertheim, M. A. Butler, K. W. West, D. N. E. Buchanan, *Rev. Sci. Instrum.* **1974**, *45*, 1369.
[80] P. E. Batson, *Phys. Rev. B* **1993**, *48*, 2608.
[81] M. A. Rampi, G. M. Whitesides, *Chem. Phys.* **2002**, *281*, 373.
[82] A. D. Becke, *J. Chem. Phys.* **1993,** *98*, 5648.
[83] A. D. Becke, *Phys. Rev. A* **1988,** *38*, 3098.
[84] C. Lee, W. Yang, R. G. Parr, *Phys. Rev. B* **1988,** *37*, 785.
[85] J. Kong, C. A. White, A. I. Krylov, D. Sherrill, R. D. Adamson, T. R. Furlani, M. S. Lee, A. M. Lee, S. R. Gwaltney, T. R. Adams, C. Ochsenfeld, A. T. B. Gilbert, G. S. Kedziora, V. A. Rassolov, D. R. Maurice, N. Nair, Y. H. Shao, N. A. Besley, P. E. Maslen, J. P. Dombroski, H. Daschel, W. M. Zhang, P. P. Korambath, J. Baker, E. F. C. Byrd, T. Van Voorhis, M. Oumi, S. Hirata, C. P. Hsu, N. Ishikawa, J. Florian, A. Warshel, B. G. Johnson, P. M. W. Gill, M. Head-Gordon, J. A. Pople, *J. Comput. Chem.* **2000,** *21*, 1532.

© 2007 WILEY-VCH Verlag GmbH & Co. KGaA, Weinheim